Research Article

ADVANCED PHOTONICS

Tunable topological polaritons by dispersion tailoring of an active metasurface

Shaojie Wang, Ke Chen,* Shufang Dong, Tian Jiang, Junming Zhao, and Yijun Feng*
Nanjing University, School of Electronic Science and Engineering, Nanjing, China

Abstract. Hyperbolic polaritons are known to exist in materials with extreme anisotropy, exhibiting exotic optical properties that enable a plethora of unusual phenomena in the fields of polaritonics and photonics. However, achieving simultaneous low-dimensionality, high-speed controllability, and on-demand reconfigurability of the polaritons remains unexplored despite their excellent potential in light–matter interactions, photonic integrated circuits, and optoelectronic devices. Here, we propose a metasurface approach to integrating artificially engineered electromagnetic anisotropy with fast-controllable electronic elements, offering a new route to realize active topological polaritons. Experiments showcase the proposed reconfigurable metasurface can support real-time transitions of designer polaritons from elliptical to flat, and then to hyperbolic and circular isofrequency contours. Correspondingly, the in-plane surface wavefront undergoes the transitions from convex to collimating, concave, and eventually back to convex. By exploiting the topological variations in polariton dispersions, we observe intriguing phenomena of controllable field canalization and tunable planar focusing. Furthermore, we report the concept of a planar reconfigurable integrated polariton circuit by spatially tailoring the distributions of polariton isofrequency contours, unveiling rich dispersion engineering possibilities and active control capabilities. We may provide an inspiring platform for developing planar active plasmonic devices with potential applications in subdiffraction-resolution imaging, sensing, and information processing.

Keywords: topological transitions; hyperbolic metasurface; anisotropic polaritons; active tuning; dispersion engineering.

Received May 4, 2024; revised manuscript received Jul. 1, 2024; accepted for publication Jul. 17, 2024; published online Aug. 19, 2024.

[DOI: 10.1117/1.AP.6.4.046005]

1 Introduction

Polaritons, the composite quasi-particles with photons stemming from strong coupling between light and collective electron oscillations, have been extensively investigated in various materials due to their unique advantages in manipulating light–matter interactions.[1–7] Recently, there has been a growing focus on emergent hyperbolic polaritons that arise in materials with extreme anisotropy, primarily due to their remarkable hyperbolic dispersion, which enables a plethora of intriguing phenomena, such as strong wave confinement, enhanced spontaneous emission, and photonic modes with large momentum, offering promising opportunities for designing advanced photonic devices.[8–12] Particularly, the phenomenon of elliptical-to-hyperbolic topological transition will occur in the extremely anisotropic medium when the polariton isofrequency contour (IFC) changes from a closed ellipse to an open hyperbola,[13] analogous to the well-known Lifshitz transition,[14] and here, the optical IFCs play the role of Fermi surface for electrons. There have been numerous demonstrations of photonic topological transition in various materials, such as van der Waals (vdW) materials,[15,16] array of graphene strips,[17,18] and optical crystals,[19,20] opening exotic avenues for the control of polaritons. In addition to naturally occurring two-dimensional materials with intrinsic hyperbolic dispersion, artificially hyperbolic metasurfaces (HMs) composed of judiciously engineered meta-atoms with in-plane anisotropy have also emerged as an exceptional platform for realizing photonic topological transition.[21–25] These HMs exhibit captivating performance due to their low-loss, simple-to-fabricate, and easy-to-integrate features. Numerous practical implementations, such as one-dimensional silver/air gratings,[26,27]

*Address all correspondence to Ke Chen, ke.chen@nju.edu.cn; Yijun Feng, yjfeng@nju.edu.cn

planar metal–dielectric–metal,[28,29] and metal–dielectric[30,31] periodic arrays supporting topological transition, have been demonstrated across optical, terahertz, and microwave frequencies.

Recently, there has been a rapidly growing interest regarding the dynamic modulation of polariton dispersion due to its excellent advantage in facilitating on-demand reconfigurability that can be harnessed for the design of advanced photonic devices. Consequently, this phenomenon has sparked widespread research into topologically reconfigurable polaritons. Many efforts have been devoted toward this goal, with two primary methodologies in general, i.e., geometry deformation and modulation of intrinsic material properties. For the geometry deformation method, the twistronics concept has played an enlightening role in polariton dispersion engineering since the discovery of flat-band superconductivity at the so-called magic angle.[32–34] Such a concept has been widely adopted in twisted-stacked bilayer configurations composed of natural hyperbolic materials[35–37] or artificial HMs,[38] leading to significant advances in realizing topologically reconfigurable polaritons associated with moiré physics. For instance, the tunable topological transitions controlled by geometric twisting operation have been demonstrated in vdW bilayer systems (such as graphene bilayers, α-MoO_3 bilayers, and others).[39–42] The modification of interlayer coupling and hybridization of wave functions between two closely spaced layers enables polariton canalization and the enhancement of light–matter interaction at the photonic magic angle and also facilitates promising interface optics applications.[40,42] In addition, the polariton dispersion can also be realized through origami deformation using three-dimensional (3D) shape-deformable metamaterials.[43] Nevertheless, the abovementioned structure-deformation-inspired topological transitions have limitations in terms of tuning speed and geometry deformation accuracy, which inevitably affect their integration into photonic integrated circuits and optoelectronic components where high-speed responsive reconfigurability and robustness are required for repeated operations. On the other hand, the active tuning on intrinsic properties of low-dimensional vdW crystals, such as refractive index and conductivity, offers a possible route to engineer anisotropic polaritons dispersion with high speed. For instance, the proposal of a graphene-covered α-MoO_3 heterostructure enables dynamic topological transition of polariton dispersions by controlling the Fermi level in the graphene layer.[37,44,45] Nevertheless, the operating wavelength of the natural hyperbolic materials is inherently limited by their crystal structure and can only be slightly tuned by environmental factors.[21] In this regard, an artificially structured HM composed of flexibly tailorable meta-atoms with desired EM properties may overcome such problems and achieve continuously controllable, high-speed responsive, and stable reconfigurability of the polariton dispersion.

Here, we propose, design, and experimentally demonstrate an electrically reconfigurable HM that enables a series of high-speed tunable polariton functionalities, including dispersion topology control, negative polariton refraction, controllable field canalization, etc. The description of "high-speed" means that the response time needed to efficiently switch different topologies of the polariton dispersions is very short. The voltage-driven varactor diode has been extensively utilized in metasurface designs, such as wireless communication,[46] information processing,[47] wave absorption,[48] digital holographs,[49] and dynamic imaging,[50] due to its inherent advantages of high-speed response and stability in practical applications. In this work, we combine the unique electrical properties of the varactor diode—especially its ability to function as a continuously tunable capacitive load—with artificial anisotropic metastructure to provide a new approach for dynamically engineering polariton dispersions. The proposed reconfigurable HM allows for real-time (switching time of 1.6 μs according to the measurements) tunable transitions from elliptical to flat and then to hyperbolic topologies, resulting in transitions from convex to collimating and concave wavefronts. Based on the topological transitions of IFCs associated with the designer polaritons, we experimentally validate controllable field canalization and tunable planar focusing. Furthermore, by spatially tailoring the distributions of polariton IFCs, we demonstrate the concept of a reconfigurable polariton circuit that facilitates flexible manipulation, guidance, and propagation of surface polaritons, unveiling rich dispersion engineering possibilities. A series of experiments is conducted in the microwave region, revealing excellent agreement between the numerical simulations and experimental measurements. Our findings may open up new avenues for achieving high-speed reconfigurable plasmonic engineering and on-chip multifunctional devices, with potential applications in high-resolution imaging, sensing, information processing, etc.

2 Results

2.1 Principle and Metasurface Design

The conceptual schematic of the HM for reconfigurable polaritons, which allows for the dynamic switching between the elliptical, flat, and hyperbolic topology of polariton dispersions under real-time control from the external voltage source, is shown in Fig. 1(a). Hence, the spatial wavefront of the surface polaritons is then changed among convex, collimating, and concave. Controlling the anisotropic properties of the metasurface is the key to realizing designer dispersion. Here, we design an anisotropic meta-atom, as shown in the inset of Fig. 1(a), which consists of a copper ground layer with a complementary rectangle-shaped ring, a substrate, a metallic hole, and a top layer with complementary H-shaped pattern. The proposed unit cell is an electromagnetic (EM) resonator, which can be equivalently regarded as an inductor-capacitor (LC) circuit where the central metal pattern mainly functions as an inductor of inductance L and the gaps between the metallic patches as capacitors of capacitance C. Obviously, the structure possesses different geometries along x and y directions due to the lack of C4 symmetry, leading to the EM anisotropy of the unit cell. Anisotropic polariton topologies arise when a surface satisfies specific constitutive parameter conditions, for example, an inductive surface with a positive imaginary part of both orthogonal conductivity components [$\mathrm{Im}(\sigma_{xx}) > 0$ and $\mathrm{Im}(\sigma_{yy}) > 0$] can support elliptical topology, while hyperbolic dispersion topology arises when the surface behaves as a capacitive and inductive one along the orthogonal direction, respectively $(\mathrm{sgn}[\mathrm{Im}(\sigma_{xx})]\cdot\mathrm{sgn}[\mathrm{Im}(\sigma_{yy})] < 0)$, according to the rigorously derived dispersion equation.[17] Analogously, the proposed unit cell with well-designed geometries can support the elliptical or hyperbolic dispersion topologies over certain frequency bands, depending on the anisotropic EM responses (or resonance properties) of the LC circuit. To this aim, an electrically driven varactor diode (namely, C_v) is loaded to the meta-atom structure, serving as the key tunable element to provide continuous control of the

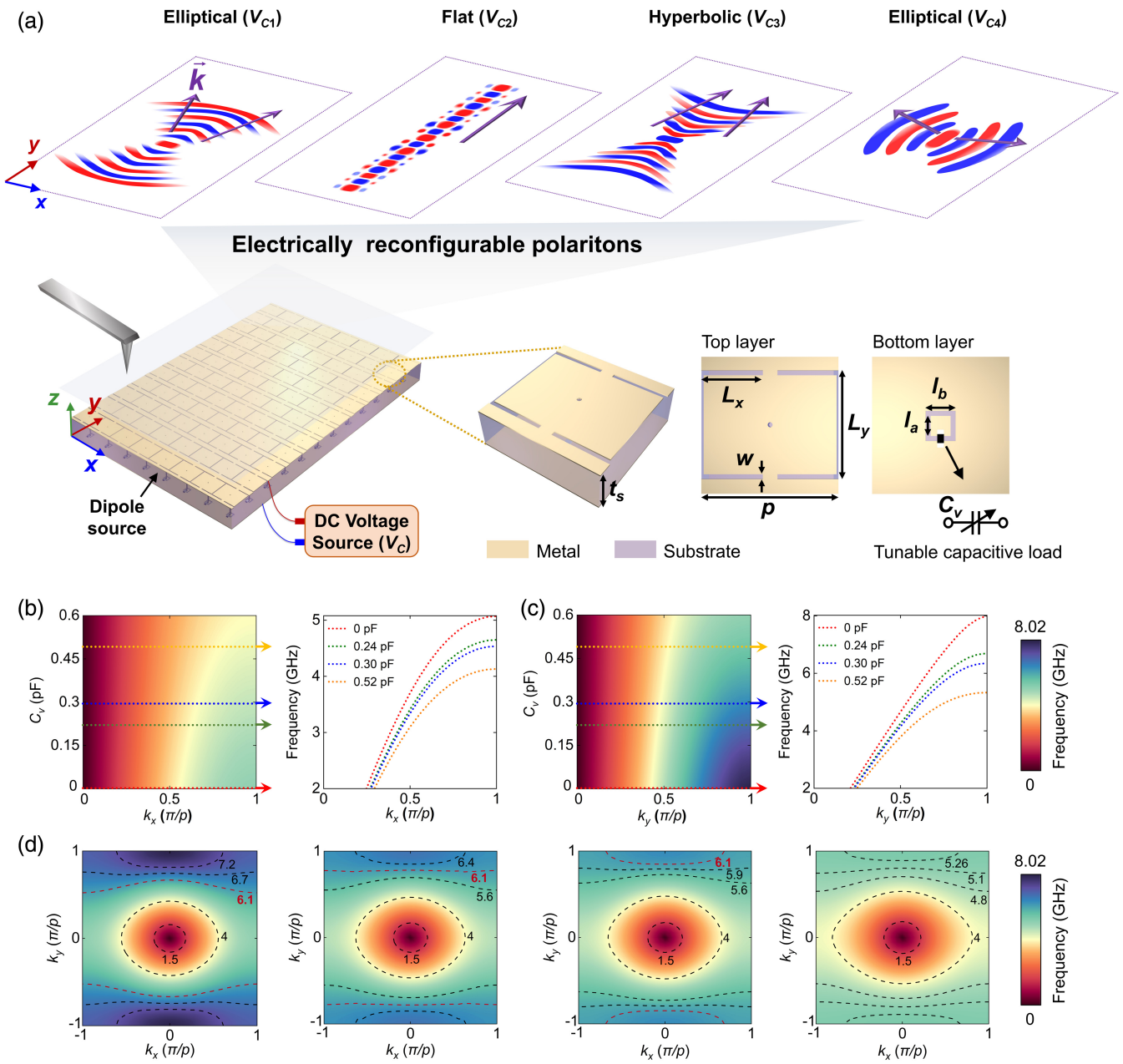

Fig. 1 Electrically reconfigurable topology of polariton dispersions with tunable metasurface. (a) Conceptual schematic of topologically reconfigurable polaritons, where the proposed reconfigurable metasurface allows for surface wavefront control from convex to collimating and eventually to concave and convex, by applying different external bias-voltage. The black arrow represents the excitation source. Bottom-right panels show the schematic of the unit cell. (b), (c) Dispersions of the polaritons along the (b) *x* and (c) *y* propagating directions. The right panels show the dispersion diagrams of the polaritons with different loaded capacitance values C_v. (d) Reconfigurable topology of IFCs of the polaritons with loaded capacitances of 0, 0.24, 0.30, and 0.52 pF, respectively. The dashed lines show the IFCs of the first band in the first Brillouin zone at different frequencies. The color maps for the dispersion of polaritons are obtained by simulations in the commercial software Computer Simulation Technology Microwave Studio.

resonance properties, thus changing the polaritons' dispersion and enabling the reconfigurable topological transition over the certain frequency band of interest. More details of the equivalent circuit analysis can be found in Sec. S1 in the Supplementary Material.

2.2 Numerical Calculation and Experimental Characterization

We numerically investigate the dispersion characteristics of the designer polaritons in reconfigurable HM by using the eigenvalue module of a commercial software Computer

Simulation Technology Microwave Studio. The optimized parameters are $p = 8.5$ mm, $L_y = 6.7$ mm, $L_x = 3.8$ mm, $w = 0.3$ mm, $l_a = 1.2$ mm, and $l_b = 1.8$ mm. The thickness of the substrate (permittivity 2.2) and copper ground layer (conductivity $\sigma = 5.96 \times 10^7$ S/m) is $t_s = 1$ mm and $t_m = 0.035$ mm, respectively. To gain an insight into the underlying mechanism, we have established the effective circuit models of the unit cell and analyzed the tunable dispersion characteristics of the polaritons, as detailed in Sec. S1 in the Supplementary Material. Based on the equivalent circuit theory, the spoof surface plasma frequencies of the designer polaritons can be calculated as the resonance frequency of the meta-atom.[28,51–53] We denote the spoof surface plasma frequencies as f_x and f_y when the polaritons propagate along the x and y directions of the meta-atom, respectively. The dispersion topologies depend on the relationship among f_0, f_x, and f_y; here, f_0 represents the observational frequency. The polaritons can propagate along both the x and y directions with the elliptical dispersion topology when $f_0 < f_x < f_y$, while a hyperbolic one can be realized when $f_x < f_0 < f_y$, and the polariton propagating along the x direction will no longer exist. The dispersions of the designer polaritons as functions of the capacitance C_v are plotted in Figs. 1(b) and 1(c). Parameters k_x and k_y represent the wave vectors of the designer polaritons along the x and y propagating directions, respectively. The dispersion diagrams with four typical capacitance values, i.e., 0, 0.24, 0.30, and 0.52 pF are illustrated in detail in the right panels of Figs. 1(b) and 1(c), where the dotted lines show unconventional dispersion effects like those natural surface plasmon polaritons with high confinement in optical frequencies. Increasing (decreasing) loaded capacitance C_v can decrease (increase) the spoof surface plasma frequencies, which are 5.07, 4.65, 4.53, and 4.13 GHz for f_x, and 8.00, 6.70, 6.35, and 5.33 GHz for f_y, with the loaded capacitance of 0, 0.24, 0.30, and 0.52 pF, respectively.

The strong in-plane anisotropy consistently occurs with various capacitance values, resulting in distinct dispersion diagrams of designer polaritons along orthogonal propagation directions. These properties can also be evidenced by the surface current distributions of the unit cell, illustrating different modes of polariton propagation along the x and y directions (see Sec. S2 in the Supplementary Material). Thus, we can flexibly engineer the dispersion properties of the unit cell and achieve reconfigurable topology of polariton dispersions. Figure 1(d) presents the polariton IFCs of the first band in the first Brillouin zone with different loaded capacitances (see Sec. S3 in Supplementary Material). As anticipated, topological transitions of the designer polaritons occur with the increase of the loaded capacitances, in which we can see obvious variation tendency of the IFCs. For instance, the red lines indicate that when the observational frequency is fixed as 6.1 GHz, the IFC curve can be sequentially changed from elliptical to flat and then hyperbolic with increasing momentum.

The polariton dispersion at 6.1 GHz is clearly presented in Fig. 2(a), where the polariton IFC starts from open elliptical topology (0 pF), to a flat line (0.24 pF), and then it changes to hyperbola (0.3 pF). Eventually, the polariton IFC features an approximate circle when the loaded capacitance C_v is changed to 0.52 pF. In this case, the IFCs of the first band in the first Brillouin zone no longer exist at 6.1 GHz [right panel of Fig. 1(d)] because the observational frequency f_0 (6.1 GHz) is larger than the spoof surface plasma frequencies of f_x (4.13 GHz) and f_y (5.33 GHz). Here, the topology of polariton dispersion is extracted from numerically simulated results of dispersion diagrams of the second band in the first Brillouin zone (see Sec. S4 in the Supplementary Material). Based on the uniaxial surface conductivity tensor, we calculated and analyzed the dispersions of the anisotropic surface based on the dispersion equations (see Sec. S5 in the Supplementary Material).

Next, we carry out numerical simulations to confirm the electrically tunable polariton dispersions, including field distributions in position space and corresponding polariton IFCs in momentum space (k-vector space) based on the proposed metasurface; here, k represents the wave vector of the designer polaritons (see Sec. S3 in the Supplementary Material). In the full-wave simulations, the metasurface consists of 54×36 unit cells with a total size of 459 mm $\times$ 306 mm. To efficiently excite the designer polaritons, a dipole source is put between the two metal layers of the unit cell located at the bottom edge of the metasurface [Fig. 1(a)].

The wavefront of the polaritons [Fig. 2(b)], obtained by full-wave simulations, undergoes intriguing transitions from convex to collimating, to concave, and eventually to convex patterns with the increase of the loaded capacitance C_v, just as indicated by the polariton IFCs.[54] The propagation characteristics of polaritons can be explained through the analysis of group velocity v_g, defined as $v_g = \partial\omega/\partial k$, which is perpendicular to the IFCs. Here, ω represents angular frequency. Thus, as shown in the left panel of Fig. 2(b), the polariton is guided into two main propagating directions when it comes to an open elliptical topology of IFC (also see Video 1 in the Appendix). When the loaded capacitance increases, the polaritons can still propagate in a splitting manner with a decreasing radiation angle. Until the flat topology of IFC appears, the second panel of Fig. 2(b) shows that the polariton propagates in a self-collimating manner without diffraction (also see Video 2 in the Appendix); such special property was originally studied in photonic crystals.[55] As the loaded capacitance C_v continues to increase, indicating extreme anisotropy of the unit cell, we can see that the polariton propagates in a convergent manner due to the hyperbolic dispersion [third panel of Fig. 2(b)], where the wavefront of the polariton is concave (also see Video 3 in the Appendix). When reaching a capacitance value of 0.52 pF [last panel of Fig. 2(b)] or larger, the polariton propagation vanishes along the y direction (see Video 4 in the Appendix). The corresponding in-plane dispersion of the designer polaritons can be intuitively viewed by the fast Fourier transform (FFT) of Re (E_z), as shown in Fig. 2(c). Topological transitions are observed in momentum space where open elliptical shapes transition into flat lines and then into open hyperbolas before closing into circles. The circle-shaped IFCs in k-vector space in first three panels of Fig. 2(c) originate from the electric fields radiated by the excitation source, which locate in the center position of k-space but with much smaller momentum than that of the designer polariton.

Experiments were conducted to validate the reconfigurable topology of polaritons using the proposed metasurface. The samples were fabricated through a standard printing circuit board technology. Complementary H-shaped patterns are periodically printed on an F4B substrate (permittivity $\varepsilon_r = 2.2$ and tangential loss $\tan\delta = 0.001$). An off-the-shelf commercial varactor diode of type MA46H120 was selected as the tunable capacitive element in each unit cell due to its flexible tunability

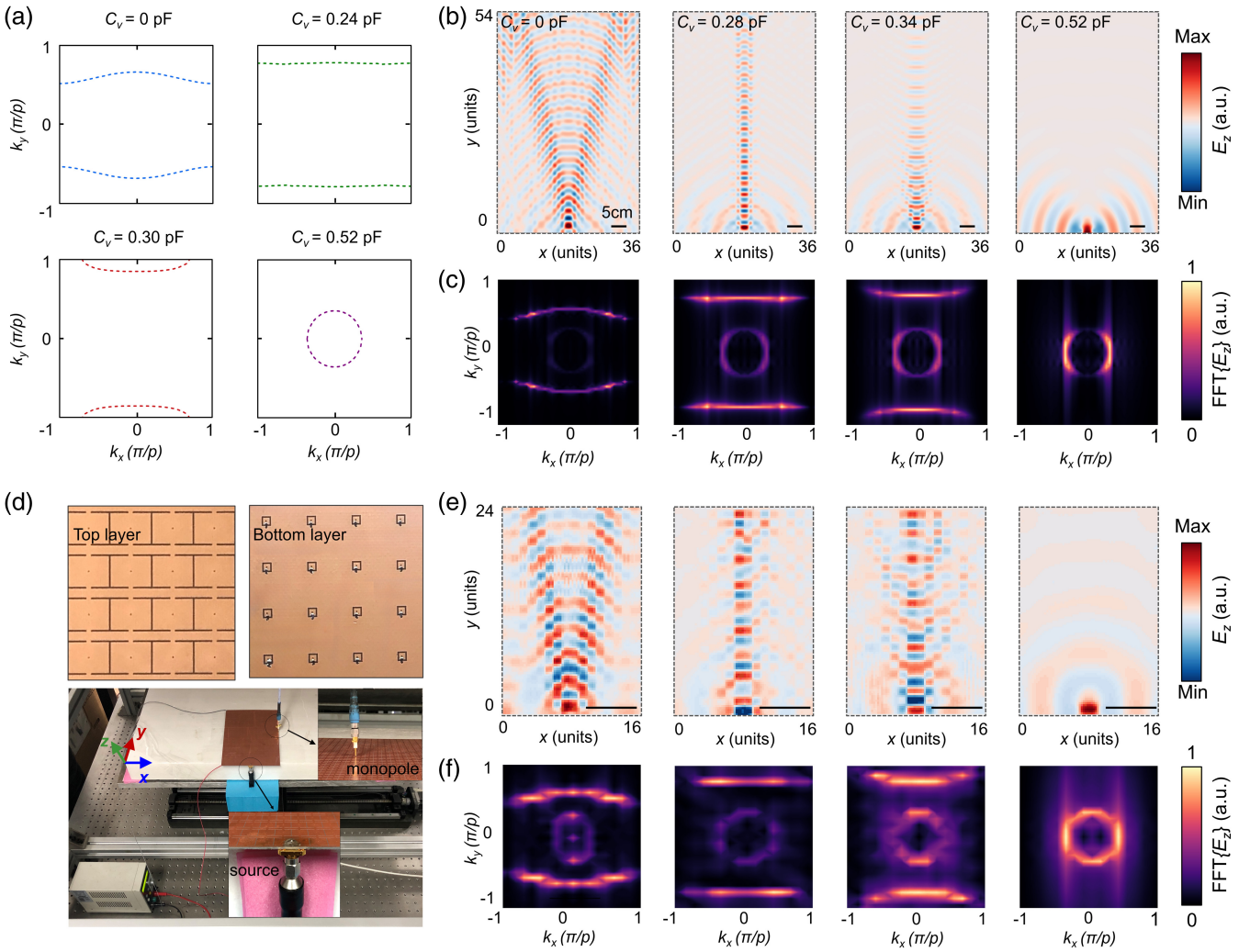

Fig. 2 Simulations and experiments of the topologically active polaritons by the proposed reconfigurable metasurface. (a) Elliptical, flat, hyperbolic, and circular topology of IFC of the polaritons at the observation frequency of 6.1 GHz. (b), (c) Simulated field distributions [real part of the z component of the electric field, Re (E_z)] in the xy plane that is 7 mm above the proposed reconfigurable metasurface (upper panels) and the corresponding dispersions in momentum space [FFT of Re (E_z)] at 6.1 GHz (bottom panels). The observation area covers 54 × 36 unit cells with a size of 459 mm × 306 mm. (d) Photograph of the fabricated sample and experimental setup. (e), (f) Measured field distributions [Re (E_z)] in the xy plane that is 1 mm above the proposed reconfigurable metasurface (upper panels) and the corresponding dispersions in momentum space [FFT of Re (E_z)] at 6.1 GHz (bottom panels). The observation area covers 24 × 16 unit cells with a size of 204 mm × 136 mm. The DC voltages are set as 8 V ($C_v = 0.25$ pF), 6.5 V ($C_v = 0.29$ pF), and 3 V ($C_v = 0.52$ pF) for the measured results of the last three columns. The abbreviation a.u. represents arbitrary units.

and stability,[56] with a tunable capacitance range from 0.149 to 1.304 pF, a parasitic resistance of <2 Ω, and a parasitic inductance of 0.05 nH extracted from the experimental measurements (see Sec. S6 in Supplementary Material).[57] The fabricated reconfigurable metasurface is composed of 24 × 16 unit cells, with a total size of 204 mm × 136 mm. Due to the limitations in achieving minimum realizable capacitance values, an additional sample composed of identical unit cells but without varactor diodes was fabricated to verify the case of $C_v = 0$ pF, namely, open elliptical topology of the polariton dispersion. In fact, there are alternative options for varactor diodes based on specific manipulation requirements, for instance, the diode type MGV125-08 (0.055 to 0.6 pF) offers a wide range of controllable capacitance, while the MAVR-011020-1411 (0.03 to 0.24 pF) covers the low capacitance region.

For the measurements, the fabricated samples are placed on a 3D movement platform, as shown in Fig. 2(d). In this setup, the top and bottom layers of the metasurface are connected to negative "−" electrode and positive "+" electrode of a DC voltage source, respectively. All the unit cells of the metasurface are in

parallel connections that share the same DC bias voltage. A subminiature version A convertor, connected to the transmitting port of the vector network analyzer (VNA), is used to connect the top and bottom layers of the metasurface to excite the polaritons propagating on the metasurface. A monopole antenna serving as the detector is connected to the receiving port of VNA for probing the electric field distributions during the sample movement. The measured electric field distributions of the metasurface are shown in Fig. 2(e), where the wavefront of the designer polariton changes from convex to collimating and to concave. Simultaneously, the corresponding polariton IFC changes from an open ellipse to a flat line and then to a hyperbola with increasing momentum in k-vector space, as shown in the first three panels of Figs. 2(e) and 2(f). In addition, a circle topology of polariton dispersion is also experimentally observed, when a large capacitance C_v is realized by applying a smaller bias voltage onto the metasurface, as shown in the last panel of Fig. 2(f). In general, it might be slightly different between the realistic capacitance and fitting value of the varactor diode due to the measurement error, as well as the fabrication tolerance of the varactor diode. Within a reasonable margin of error, the measured results are consistent with the simulated results, fully validating the reconfigurable topological transition of the metasurface polaritons. In addition, experimental measurements demonstrate that the response time of the topology switching is around 1.6 μs, enabling high-speed responsive reconfigurability of the proposed metasurface (see Sec. S7 in the Supplementary Material).

2.3 Controllable Field Canalization and Tunable Planar Focusing

As the polariton propagation is highly correlated with the dispersion characteristic that can be flexibly manipulated at a certain frequency band, the proposed reconfigurable metasurface may find plenty of applications for polariton manipulation. As the proof of concept, we here experimentally present and discuss the intriguing phenomena of controllable field canalization and tunable planar focusing enabled by the tunable polariton dispersions. When the polariton dispersion is switched to flat line fashion, the metasurface can yield diffraction-free propagation wave due to the flat topology of IFC [the second column of Fig. 2(b)]. This phenomenon is known as canalized propagation,[39,58–60] with excellent potential in realizing hyperlensing,[10,61] subdiffraction-resolution imaging,[26] retroreflection,[62] and position sensing.[63] Here, the proposed reconfigurable metasurface benefits from the utilization of voltage-controllable varactor diodes, enabling us to achieve a broad bandwidth of field canalization. Figure 3(a) clearly depicts the topological transition regions as functions of frequency and loaded capacitance C_v, in which blue, light green, and red regions represent the closed elliptical, open elliptical, and hyperbolic polariton dispersions, respectively. The gray region denotes that the polariton IFCs of the first band in the first Brillouin zone no longer exist. For a fixed capacitance or bias voltage, we can only observe the field canalization phenomena in a very limited frequency band, due to the inherent dispersion of the metasurface structure. Differently, by adaptively applying different bias voltage, such dispersion can be counteracted to yield canalization propagation with enhanced bandwidth, as depicted by the green dashed line, the presence of flat polariton IFCs. The green circles in Fig. 3(a) denote the measured canalization points under different bias voltages. Figure 3(b) shows the measured electric field distributions at 5.5 GHz ($V_C = 4$ V, $C_v = 0.42$ pF), 5.9 GHz ($V_C = 6$ V, $C_v = 0.31$ pF), 6.2 GHz ($V_C = 10$ V, $C_v = 0.21$ pF), and 6.3 GHz ($V_C = 12$ V, $C_v = 0.19$ pF), where we observe obviously the polaritons propagating in a self-collimating manner at different frequencies. More simulated and measured results can be found in the Supplementary Material (see Sec. S8 in the Supplementary Material). Considering the ohmic loss of the parasitic resistance of the varactor diode, detailed information about the propagation loss of the field canalization mode is further provided (see Sec. S9 in the Supplementary Material).

As the landmark feature of hyperbolic polaritons, hyperbolic dispersion has garnered significant attention due to its exotic optical properties and potential applications in all-angle negative refraction,[27,64] planar focusing,[28,30] waveguiding,[65] and spin control.[66] Here, we demonstrate tunable planar focusing based on the proposed reconfigurable metasurface. Figure 3(c) presents the schematic of the tunable polariton focusing, where light blue and light yellow blocks are the reconfigurable metasurface and air regions, respectively, and the green dashed circle placed at the bottom side of the metasurface represents the excitation source. The metasurface is switched to the state of hyperbolic dispersion by the bias voltage. The propagation directions of the polariton, illustrated by the red arrows, are included within the IFCs to schematically show the dispersion-induced hyperbolic propagation, which will be focused into a hotspot as the polariton propagates into the surrounding air medium. Measurements are conducted in the air region represented by the red dotted frame to confirm the tunable planar focusing and excellent performance can be observed from 6.04 to 6.6 GHz. Figure 3(d) presents the measured intensity distributions ($|E_z|^2$) at 6.1 GHz ($V_C = 6$ V, $C_v = 0.31$ pF), 6.3 GHz ($V_C = 7.3$ V, $C_v = 0.27$ pF), 6.43 GHz ($V_C = 8.8$ V, $C_v = 0.23$ pF), and 6.6 GHz ($V_C = 11.8$ V, $C_v = 0.19$ pF), where the efficient energy focusing of the designed polaritons is verified by the focal points in the air, with a full width at half-maximum of around 0.5 λ. More simulated and measured results are provided in the Supplementary Material (see Sec. S10 in the Supplementary Material).

2.4 Planar Reconfigurable Integrated Polariton Circuit

Furthermore, the proposed metasurface can realize the concept of planar reconfigurable polariton circuits, where the individual control of each meta-atom IFC is achieved through external voltages. This allows for regional control over the dispersion curves of the meta-atoms and enables the combination of different anisotropic topologies to generate intriguing polariton functions. As the design examples, Fig. 4(a) shows the schematic of the planar reconfigurable polariton circuit composed of two different metasurface regions. The blue and orange blocks represent the arrays of unit cells with the loaded capacitance of C_{v1} and C_{v2}, respectively, which can be realized by applying different voltages on the corresponding regions. At the interface [dashed line in Fig. 4(a)] of two regions, the on-demand manipulation and guidance of propagation of polaritons can be engineered by tailoring the distributions of topologies of polariton dispersions with flexibility and diversity. The green dashed circle is the excitation source placed at the bottom side of the metasurface. Simulations of several extraordinary propagation phenomena are conducted at 6.1 GHz, as shown in

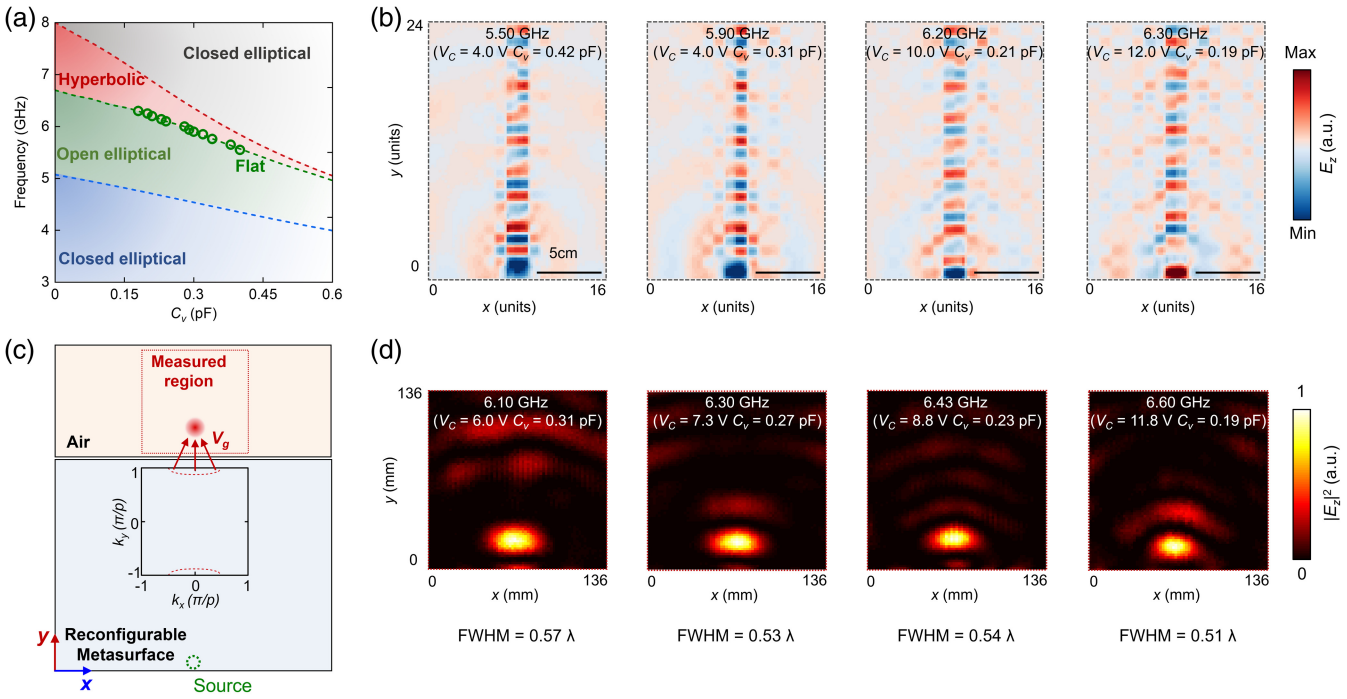

Fig. 3 Controllable field canalization and tunable planar focusing based on topological transition of polariton dispersions. (a) Topological transition regions as a function of frequency and loaded capacitance value C_v, which is extracted from the numerical simulations of dispersion diagrams of both the first and the second band in the first Brillouin zone. (b) Measured field distributions [Re (E_z)] in the xy plane that is 1 mm above the reconfigurable metasurface at different frequencies. The observation areas consist of 24 × 16 unit cells with a size of 204 mm × 136 mm. (c) Schematic of the planar focusing as the polaritons propagate from the metasurface into the surrounding air medium. The inset shows the hyperbolic topology of polariton dispersion at 6.1 GHz with the $C_v = 0.32$ pF. The red arrows indicate the propagation directions of the polaritons and the red dot represents the focal point. (d) Measured intensity distributions ($|E_z|^2$) in the xy plane that is 1 mm above the reconfigurable HM at different frequencies. The observation areas have a size of 136 mm × 136 mm.

Figs. 4(b)–4(d). The polariton IFCs in two regions are presented in the right panels, where the black solid arrows represent the group velocity v_g, corresponding to the propagation directions of designer polaritons (black dotted arrows in left panels). As shown in Fig. 4(b), the negative refraction occurs at the interface when the polariton IFC is set to be hyperbolic dispersion in region 2 (also see Video 5 in the Appendix). Figure 4(c) shows the wave-splitting functionality (also see Video 6 in the Appendix), where the designer polariton propagates along two symmetric directions at the interface by combining the open elliptical and flat topology of polariton dispersions. In contrast, the polariton propagation can be suppressed along the y direction when the varactor diodes of region 2 are tuned as large capacitance value (e.g., $C_v = 0.52$ pF in Fig. 2), as shown in Fig. 4(d). In this case, the collimating wavefront is launched on region 1 and propagates toward region 2, but eventually spreads out as convex wavefront in region 2 (also see Video 7 in the Appendix). It should be noted that the proposed reconfigurable integrated polariton circuit in Fig. 4(a) is a reciprocal system, and the demonstrated transformation of the polariton propagation regimes in Figs. 4(b)–4(d) is still feasible in reverse. In addition to the results presented above, other functionalities for manipulation of polaritons can be realized, such as collimating refraction [see Fig. S16(a) in Sec. S11 in the Supplementary Material and also Video 8 in the Appendix] and the suppression of polariton propagation for convex wavefront [see Fig. S16(b) in Sec. S11 in the Supplementary Material and also Video 9 in the Appendix]. These results show promise for their use in designing reconfigurable spatial multiplexers. Notably, unlike the passive metasurfaces where polariton propagation is fixed once fabricated, our designs offer on-demand reconfigurability through voltage-driven electronic elements, which represents a fundamental difference from the existing approaches. Serving as the illustration examples, here we only consider the proposed reconfigurable polariton circuit composed of two different regions of unit cells for simplification. In fact, there is much potential for other extraordinary propagation phenomena of polaritons and advanced functions by a polariton circuit with more complex combination of topologies of polariton dispersion (see Sec. S12 in the Supplementary Material), and even by a planar programmable integrated polariton circuit (see Sec. S13 in Supplementary Material). Particularly for the planar programmable integrated polariton circuit, a series of cases for polariton propagation (supporting multi-excitation sources, multi-ports, and flexibly designable propagation routes) has been designed and simulated, which significantly expanded the possibilities for polariton manipulation and guidance and may shed new light on the design of subwavelength surface

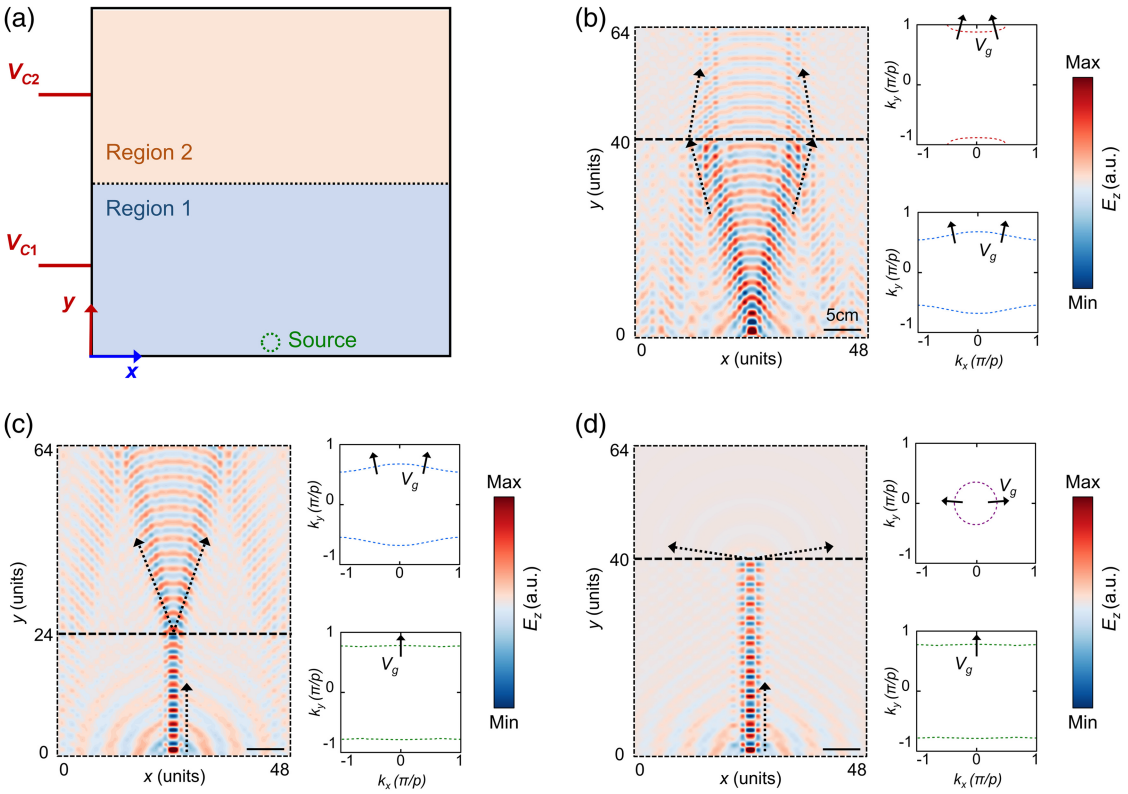

Fig. 4 Reconfigurable integrated polariton circuit. (a) Schematic of the planar reconfigurable polariton circuit composed of two regions (region 1 and region 2) represented by blue and orange blocks, respectively. The loaded capacitances of unit cells are different in region 1 and region 2, leading to different topologies of polariton dispersions. (b)–(d) Simulated field distributions [Re (E_z)] in the xy plane that is 7 mm above the polariton circuit. The right panels show the polariton IFCs in two different regions. The loaded capacitances in region 1 and region 2 are (b) 0.03 and 0.32 pF for realizing the negative refraction, (c) 0.28 and 0.03 pF for realizing the wave splitting, and (d) 0.28 and 0.52 pF for realizing the suppression of polariton propagation. The green dashed circle represents the excitation source. The dotted lines indicate the main propagating directions of the polaritons. The observation areas consist of 64 × 48 unit cells with a size of 544 mm × 408 mm.

waveguides. The proposed metasurface that supports topologically reconfigurable polaritons makes it a promising candidate for on-chip advanced photonics systems and may shed new light on designing planar multifunctional plasmonic devices and integrated optoelectronic circuits, etc.

3 Discussion

Here, we propose, fabricate, and experimentally demonstrate topologically reconfigurable polaritons over a varactor diode-based tunable metasurface. The combination of a continuously tunable capacitive diode with judicious metastructure anisotropy presents a new strategy for electrically engineering the polariton dispersions, revealing topological transitions from elliptical to flat, hyperbolic, and circular IFCs, as well as functional designs of controllable field canalization and planar focusing. Compared with previous methods related to dynamic modulation of polaritons, our work features continuous controllability and particularly supports high switching speed of reconfigurable polaritons, making it more appealing for practical applications. We further report the concept of reconfigurable polariton circuit that enables engineered topologies of polariton dispersions on demand, thus realizing flexible manipulation, guidance, and propagation of polaritons. The great potential of the proposed reconfigurable HM in dispersion and active engineering may inspire novel programmable plasmonic circuits. Although demonstrated at microwave frequencies, the concept of electrically tunable polaritons can also be applied to higher frequencies, such as millimeter-wave and terahertz-wave, by possibly using millimeter-wave semiconductor diodes[67] and liquid crystals.[68] With the advancement in on-chip polaritonics, we anticipate that the proposed methodology for actively engineering topological polariton and the concept of planar programmable integrated polariton circuit may offer an untapped platform toward on-chip advanced polaritonics and photonics for interface optics applications, with potential applications in high-resolution imaging systems, subwavelength surface waveguides, multichannel power dividers, information processing, and other functional devices.

4 Appendix: Supplementary Videos

Video 1. Propagation of polariton with the open-elliptical topology of IFC over reconfigurable HM, as shown in the first panel of Fig. 2(b) (MP4, 1.01 MB [URL: https://doi.org/10.1117/1.AP.6.4.046005.s1]).

Video 2. Propagation of polariton with flat topology of IFC over reconfigurable HM, as shown in the second panel of Fig. 2(b) (MP4, 864 KB [URL: https://doi.org/10.1117/1.AP.6.4.046005.s2]).
Video 3. Propagation of polariton with hyperbolic topology of IFC over reconfigurable HM, as shown in the third panel of Fig. 2(b) (MP4, 920 KB [URL: https://doi.org/10.1117/1.AP.6.4.046005.s3]).
Video 4. Propagation of polariton with circular topology of IFC over reconfigurable HM, as shown in the last panel of Fig. 2(b) (MP4, 544 KB [URL: https://doi.org/10.1117/1.AP.6.4.046005.s4]).
Video 5. Negative refraction of polariton over reconfigurable polariton circuit, as shown in Fig. 4(b) (MP4, 1.06 MB [URL: https://doi.org/10.1117/1.AP.6.4.046005.s5]).
Video 6. Polariton splitting over reconfigurable polariton circuit, as shown in Fig. S4(c) in the Supplementary Material (MP4, 1.05 MB [URL: https://doi.org/10.1117/1.AP.6.4.046005.s6]).
Video 7. Suppression of polariton propagation for collimating wavefront over reconfigurable polariton circuit, as shown in Fig. 4(d) (MP4, 756 KB [URL: https://doi.org/10.1117/1.AP.6.4.046005.s7]).
Video 8. Collimating refraction of polariton over reconfigurable polariton circuit, as shown in Fig. S10(a) in the Supplementary Material (MP4, 1.06 MB [URL: https://doi.org/10.1117/1.AP.6.4.046005.s8]).
Video 9. Suppression of polariton propagation for convex wavefront over reconfigurable polariton circuit, as shown in Fig. S10(b) in the Supplementary Material (MP4, 1.08 MB [URL: https://doi.org/10.1117/1.AP.6.4.046005.s9]).

Disclosures

The authors declare that they have no competing interests.

Code and Data Availability

All other data that support the findings of this study are available from the corresponding authors upon reasonable request.

Acknowledgments

This work was supported by the National Natural Science Foundation of China (NSFC) (Grant Nos. 62271243 and 62071215), the Fundamental Research Funds for the Central Universities, the Jiangsu Provincial Key Research and Development Program (Grant No. BE2023084), the Priority Academic Program Development of Jiangsu Higher Education Institutions, and the Jiangsu Provincial Key Laboratory of Advanced Manipulating Technique of Electromagnetic Wave. All authors contributed extensively to the work presented in this paper. Conceptualization, S.W. and K.C.; methodology, S.W. and K.C.; investigation, S.W. and F.D.; visualization, S.W. and K.C.; supervision, K.C. and Y.F.; writing—original draft, S.W. and K.C.; writing—review and editing, S.W., K.C., F.D., T.J., J.Z., and Y.F.

References

1. J. Lin et al., "Polarization-controlled tunable directional coupling of surface plasmon polaritons," *Science* **340**(6130), 331–334 (2013).
2. G. Hu et al., "Phonon polaritons and hyperbolic response in van der Waals materials," *Adv. Opt. Mater.* **8**(5), 1901393 (2020).
3. Z. Fei et al., "Nano-optical imaging of WSe_2 waveguide modes revealing light-exciton interactions," *Phys. Rev. B* **94**(8), 081402 (2016).
4. X. Liu et al., "Strong light-matter coupling in two-dimensional atomic crystals," *Nat. Photonics* **9**(1), 30–34 (2014).
5. J. Chen et al., "Optical nano-imaging of gate-tunable graphene plasmons," *Nature* **487**(7405), 77–81 (2012).
6. S. Dai et al., "Tunable phonon polaritons in atomically thin van der Waals crystals of boron nitride," *Science* **343**(6175), 1125–1129 (2014).
7. Z. Cai et al., "Polariton photonics using structured metals and 2D materials," *Adv. Opt. Mater.* **8**(5), 1901090 (2020).
8. P. Huo et al., "Hyperbolic metamaterials and metasurfaces: fundamentals and applications," *Adv. Opt. Mater.* **7**(14), 1801616 (2019).
9. A. Poddubny et al., "Hyperbolic metamaterials," *Nat. Photonics* **7**, 948–957 (2013).
10. L. Ferrari et al., "Hyperbolic metamaterials and their applications," *Prog. Quantum Electron.* **40**, 1–40 (2015).
11. P. Li et al., "Infrared hyperbolic metasurface based on nanostructured van der Waals materials," *Science* **359**(6378), 892–896 (2018).
12. A. Nemilentsau et al., "Switchable and unidirectional plasmonic beacons in hyperbolic two-dimensional materials," *Phys. Rev. B* **99**(20), 201405 (2019).
13. H. N. S. Krishnamoorthy et al., "Topological transitions in metamaterials," *Science* **336**(6078), 205–209 (2012).
14. I. M. Lifshitz, "Anomalies of electron characteristics of a metal in the high pressure region," *Sov. Phys. JETP* **11**, 1130 (1960).
15. D. Correas-Serrano et al., "Black phosphorus plasmonics: anisotropic elliptical propagation and nonlocality-induced canalization," *J. Opt.* **18**(10), 104006 (2016).
16. C. Wang et al., "Van der Waals thin films of WTe_2 for natural hyperbolic plasmonic surfaces," *Nat. Commun.* **11**(1), 1158 (2020).
17. J. S. Gomez-Diaz, M. Tymchenko, and A. Alu, "Hyperbolic plasmons and topological transitions over uniaxial metasurfaces," *Phys. Rev. Lett.* **114**(23), 233901 (2015).
18. J. S. Gomez-Diaz, M. Tymchenko, and A. Alù, "Hyperbolic metasurfaces: surface plasmons, light-matter interactions, and physical implementation using graphene strips [Invited]," *Opt. Mater. Express* **5**(10), 2313–2329 (2015).
19. W. Ma et al., "Ghost hyperbolic surface polaritons in bulk anisotropic crystals," *Nature* **596**(7872), 362–366 (2021).
20. N. C. Passler et al., "Hyperbolic shear polaritons in low-symmetry crystals," *Nature* **602**(7898), 595–600 (2022).
21. D. Lee et al., "Hyperbolic metamaterials: fusing artificial structures to natural 2D materials," *eLight* **2**(1), 1 (2022).
22. J. S. Gomez-Diaz and A. Alù, "Flatland optics with hyperbolic metasurfaces," *ACS Photonics* **3**(12), 2211–2224 (2016).
23. Z. Guo, H. Jiang, and H. Chen, "Hyperbolic metamaterials: from dispersion manipulation to applications," *J. Appl. Phys.* **127**(7), 071101 (2020).
24. O. Y. Yermakov et al., "Hybrid waves localized at hyperbolic metasurfaces," *Phys. Rev. B* **91**(23), 235423 (2015).
25. P. Zheng et al., "Anomalous wave propagation in topological transition metasurfaces," *Adv. Opt. Mater.* **7**(11), 1801483 (2019).
26. A. A. High et al., "Visible-frequency hyperbolic metasurface," *Nature* **522**(7555), 192–196 (2015).
27. Y. Liu and X. Zhang, "Metasurfaces for manipulating surface plasmons," *Appl. Phys. Lett.* **103**, 141101 (2013).
28. Y. Yang et al., "Hyperbolic spoof plasmonic metasurfaces," *NPG Asia Mater.* **9**(8), e428 (2017).
29. H. Chen et al., "Efficient manipulation of spoof surface plasmon polaritons based on rotated complementary h-shaped resonator metasurface," *IEEE Trans. Antennas Propag.* **65**(12), 7383–7388 (2017).

30. Y. Yang et al., "Magnetic hyperbolic metasurface: concept, design, and applications," *Adv. Sci.* **5**(12), 1801495 (2018).
31. O. V. Kotov and Y. E. Lozovik, "Hyperbolic hybrid waves and optical topological transitions in few-layer anisotropic metasurfaces," *Phys. Rev. B* **100**(16), 165424 (2019).
32. Y. Cao et al., "Correlated insulator behaviour at half-filling in magic-angle graphene superlattices," *Nature* **556**(7699), 80–84 (2018).
33. J. M. Park et al., "Tunable strongly coupled superconductivity in magic-angle twisted trilayer grapheme," *Nature* **590**(7845), 249–255 (2021).
34. Y. Cao et al., "Unconventional superconductivity in magic-angle graphene superlattices," *Nature* **556**(7699), 43–50 (2018).
35. J. Duan et al., "Twisted nano-optics: manipulating light at the nanoscale with twisted phonon polaritonic slabs," *Nano Lett.* **20**(7), 5323–5329 (2020).
36. A. Nemilentsau, T. Low, and G. Hanson, "Anisotropic 2D materials for tunable hyperbolic plasmonics," *Phys. Rev. Lett.* **116**(6), 066804 (2016).
37. Z. Cai et al., "Tunable optical forces enabled by bilayer van der Waals materials," *Adv. Opt. Mater.* **12**(1), 2301288 (2024).
38. Y. Liu et al., "Moiré-driven electromagnetic responses and magic angles in a sandwiched hyperbolic metasurface," *Photonics Res.* **10**(9), 2056–2065 (2022).
39. G. Hu et al., "Moiré hyperbolic metasurfaces," *Nano Lett.* **20**(5), 3217–3224 (2020).
40. G. Hu et al., "Enhanced light-matter interactions at photonic magic-angle topological transitions," *Appl. Phys. Lett.* **118**(21), 211101 (2021).
41. G. Hu et al., "Topological polaritons and photonic magic angles in twisted α-MoO_3 bilayers," *Nature* **582**(7811), 209–213 (2020).
42. Q. Zhang et al., "Interface nano-optics with van der Waals polaritons," *Nature* **597**(7875), 187–195 (2021).
43. M. Li et al., "Topologically reconfigurable magnetic polaritons," *Sci. Adv.* **8**(50), eadd6660 (2022).
44. G. Álvarez-Pérez et al., "Active tuning of highly anisotropic phonon polaritons in van der Waals crystal slabs by gated grapheme," *ACS Photonics* **9**(2), 383–390 (2022).
45. H. Hu et al., "Gate-tunable negative refraction of mid-infrared polaritons," *Science* **379**(6632), 558–561 (2023).
46. W. Tang et al., "Wireless communications with programmable metasurface: transceiver design and experimental results," *China Commun.* **16**(5), 46–61 (2019).
47. L. Li and T. J. Cui, "Information metamaterials: from effective media to real-time information processing systems," *Nanophotonics* **8**(5), 703–724 (2019).
48. J. Zhang et al., "Electrically tunable metasurface with independent frequency and amplitude modulations," *ACS Photonics* **7**(1), 265–271 (2019).
49. R. Feng et al., "Reprogrammable digital holograms and multibit spatial energy modulation using a reflective metasurface," *ACS Appl. Electron. Mater.* **3**(12), 5272–5277 (2021).
50. K. Chen et al., "A reconfigurable active Huygens' metalens," *Adv. Mater.* **29**(17), 1606422 (2017).
51. J. B. Pendry, L. Martín-Moreno, and F. J. Garcia-Vidal, "Mimicking surface plasmons with structured surfaces," *Science* **305**(5685), 847–848 (2004).
52. A. P. Hibbins, B. R. Evans, and J. R. Sambles, "Experimental verification of designer surface plasmons," *Science* **308**(5722), 670–672 (2005).
53. H. Su et al., "Efficient generation of microwave plasmonic vortices via a single deep-subwavelength meta-particle," *Laser Photonics Rev.* **12**(9), 1800010 (2018).
54. G. Dolling et al., "Simultaneous negative phase and group velocity of light in a metamaterial," *Science* **312**(5775), 892–894 (2006).
55. J. Witzens, M. Loncar, and A. Scherer, "Self-collimation in planar photonic crystals," *IEEE J. Sel. Top. Quantum Electron.* **8**(6), 1246–1257 (2002).
56. MACOM Technology Solutions, "MA46H120 Varactor Datasheet [Online]," https://cdn.macom.com/datasheets/MA46H120%20Series.pdf (accessed 7 April 2024).
57. N. Nguyen-Trong et al., "Analysis and design of a reconfigurable antenna based on half-mode substrate-integrated cavity," *IEEE Trans. Antennas Propag.* **63**(8), 3345–3353 (2015).
58. P. Li et al., "Collective near-field coupling and nonlocal phenomena in infrared-phononic metasurfaces for nano-light canalization," *Nat. Commun.* **11**(1), 3663 (2020).
59. D. Correas-Serrano, A. Alù, and J. S. Gomez-Diaz, "Plasmon canalization and tunneling over anisotropic metasurfaces," *Phys. Rev. B* **96**(7), 075436 (2017).
60. O. Yermakov et al., "Surface waves on self-complementary metasurfaces: all-frequency hyperbolicity, extreme canalization, and TE-TM polarization degeneracy," *Phys. Rev. X* **11**(3), 031038 (2021).
61. X. Zhang and Z. Liu, "Superlenses to overcome the diffraction limit," *Nat. Mater.* **7**(6), 435–441 (2008).
62. L.-Z. Yin et al., "Ultrathin all-angle hyperbolic metasurface retroreflectors based on directed routing of canalized plasmonics," *ACS Appl. Electron. Mater.* **14**(18), 21605–21612 (2022).
63. C. Hu et al., "A metasurface with bidirectional hyperbolic surface modes and position-sensing applications," *NPG Asia Mater.* **10**(5), 417–428 (2018).
64. J. Yao et al., "Optical negative refraction in bulk metamaterials of nanowires," *Science* **321**(5891), 930 (2008).
65. Y. Yang et al., "Type-I hyperbolic metasurfaces for highly-squeezed designer polaritons with negative group velocity," *Nat. Commun.* **10**(1), 2002 (2019).
66. O. Y. Yermakov et al., "Spin control of light with hyperbolic metasurfaces," *Phys. Rev. B* **94**(7), 075446 (2016).
67. M. T. Nouman et al., "Terahertz modulator based on metamaterials integrated with metal-semiconductor-metal varactors," *Sci. Rep.* **6**(1), 26452 (2016).
68. S. Wang et al., "Tunable non-diffraction spoof surface plasmon polaritons with liquid crystal terahertz metasurface," in *IEEE MTT-S Int. Microw. Workshop Series on Adv. Mater. and Processes for RF and THz Appl. (IMWS-AMP)* (2021).

Shaojie Wang received his BE degree in electronic science and engineering from Xiamen University, Xiamen, China, in 2020. He is currently pursuing his PhD in electronic science and engineering with Nanjing University, Nanjing, China. His current research focuses on the dispersion tailoring of metasurfaces and metagrating, as well as their applications to novel microwave and photonic devices.

Ke Chen received his BS and PhD degrees in electronic science and engineering from Nanjing University, Nanjing, China, in 2012 and 2017, respectively. He is currently an associate professor at the Department of Electronic Engineering, School of Electronic Science and Engineering, Nanjing University. His research interests include electromagnetic metamaterials and metasurfaces and their microwave and photonic applications. He has hosted more than 10 research projects and published over 100 journal papers.

Shufang Dong received her BE degree in electronic science and engineering from Xiamen University, Xiamen, China, in 2018. She is currently pursuing her PhD in electronic science and engineering with Nanjing University, Nanjing, China. Her current research focuses on full-space multiplexing electromagnetic control and wireless communication based on directional Janus metasurfaces.

Tian Jiang received his MSc and PhD degrees from the Department of Electronic Science and Engineering, Nanjing University, Nanjing, China, in 2004 and 2007, respectively. Since 2007, he has been a faculty member and currently a professor at the Department of Electronic Engineering, School of Electronic Science and Engineering, Nanjing University. His research interests include electromagnetic metasurfaces and their application to microwave and photonic devices.

Junming Zhao received his BS and PhD degrees in electronic science and engineering from Nanjing University, Nanjing, China, in 2003 and 2009, respectively. Since 2009, he has been a faculty member at the Department of Electronic Engineering, School of Electronic Science and Engineering, Nanjing University, where he is currently a professor. His research interests include electromagnetic metamaterials and metasurfaces and their applications to novel microwave functional devices.

Yijun Feng received his PhD from Nanjing University in 1992 and is currently a full professor at Nanjing University. His research interests include electromagnetic metamaterials and their application to microwave and photonic devices, electromagnetic wave theory, and novel microwave functional materials. He has received the 2010 Science and Technology Award (First Grade) of Jiangsu Province, 2021 Science and Technology Award (First Grade) of Shanxi Province, and the 2022 Natural Science Award (First Grade) of Chinese Institute of Communication. He has authored or co-authored over 200 peer-reviewed journal papers and over 160 refereed international conference papers.